# Composed Segmentation of Tubular Structures by an Anisotropic PDE Model

Elena Franchini, Serena Morigi, and Fiorella Sgallari

Department of Mathematics-CIRAM, University of Bologna, Bologna, Italy
{franchini,morigi,sgallari}@dm.unibo.it

**Abstract.** In this work we introduce the composed segmentation (C-segmentation), that is a priori composition of sources to obtain a single one segmentation result according to specific logic combinations. The approach and the segmentation model are general but we apply the C-segmentation technique to the challenging problem of segmenting tubular-like structures. The reconstruction is obtained by continuously deforming an initial distance function following the Partial Differential Equation (PDE)-based diffusion model derived from a minimal volume-like variational formulation. The gradient flow for this functional leads to a nonlinear curvature motion model. An anisotropic variant is provided which includes a diffusion tensor aimed to follow the tube geometry. Numerical examples demonstrate the ability of the proposed method to produce high quality 2D/3D segmentations of complex and eventually incomplete synthetic and real data.

## 1 Introduction

Segmentation of three-dimensional (3D) images can be a very useful computer aided diagnosis tool for clinical routines or surgical planning. We use the term *composed segmentation* for systems that extract structures from several images, by combining them according to specific Boolean operations. Traditionally, the segmentation process independently performed on single images have to be combined by cumbersome algorithms. The goal of C-segmentation is to combine complementary multispatial, multisensor, multitemporal and/or multiview information into one new domain containing only the information to be segmented. The term composed means by Boolean operations which depends on the application requirements. The individual images entering the C-segmentation process need to be registered to a common frame of reference, this is a nontrivial task which could affect the robustness of the segmentation approach, but it is not addressed in this work. We assume the input images have been preliminary registered.

Let us illustrate the role of C-segmentation in different applications. Multimodal fusion deals with images that capture different physical properties of the original scene. In this case, C-segmentation identifies and segments the union of regions of interest. Multispatial fusion is related to several images which cover a single one scene, for example several aerial photographs to represent an entire territorial region, or multiple CT scans to reconstruct a human organ. The

X.-C. Tai et al. (Eds.): SSVM 2009, LNCS 5567, pp. 75–86, 2009.
© Springer-Verlag Berlin Heidelberg 2009

C-segmentation unifies all the information, eventually replicated in the multiple sources, into a single one segmented structure. Multitemporal composition requires the comparison between images representing the same structures acquired at different timing. For example, in medical analysis, a tumor-region growing is monitored by subsequently images of the region of interest. The C-segmentation can identify and segment the difference between structures in two images, reconstructing the grown area.

While our segmentation methodology is quite general, we focus our attention on the most challenging problem of tubular-like segmentation which is particularly difficult in case of multiple sources due to the huge amount of connected structures that should be reconstructed. In particular, we will consider applications in medical image analysis which are interested in the extraction of anatomical surfaces of tubular structures like blood vessels. Indeed, problems like aneurysm or stenosis can occur in a vessel, and the clinicians need tools to help them in interpreting and quantifying the images for evaluating the pathology, for proposing a therapy or a surgical operation, for planning minimally invasive treatment.

A number of deformable model-based approaches for vessel segmentation or, generally tube-like structures, have received considerable attention and success. We refer the reader to [4] for an extended review on vessel segmentation algorithms. Since explicit deformable model representation is usually impractical, level set techniques to evolve a deformable model have been recently introduced, which provide implicit representation of a deformable model. A curve in 2D or a surface in 3D evolves in such a way as to cover a complex shape or structure. Its initialization can be either manual or automatic and it needs not to be close to the desired solution. A disadvantage of level sets segmentation approach is the computational effort required to cover the entire domain of interest which is, in general, one dimension higher than the original one. Interested readers are referred to recent literature on the level set segmentation strategy for tubular structures [5], [6], [7], [8], [10]. A generalization of the single-channel active contour without edges model is proposed in [9] for object detection using logic operations. This logic framework suffers from the active contour model limits, and is not suitable for detecting tubular structures.

In this work, we modify a geometric deformable model segmentation procedure based on level sets [2], to obtain a fast and accurate method for solving the C-segmentation problem to extract tubular structures from multiple 2D/3D images, and we apply the proposed segmentation method for segmenting blood vessels, neurovascular structures and similar characteristics medical images. The main contributions of this work concern the design of a strategy to deal with directionality in the vessels based on a diffusion tensor, and the capability to compose segmentation of multiple images according to Boolean operations. The former makes the segmentation algorithm able to follow tubular structures and connect eventually disconnected parts, while the latter let simultaneously combine different information into a robust segmentation method. The proposed method is able to segment twisted, convoluted, and occluded structures without

the user interactivity, following branching of different layers, from thinner to larger structures. One of the major disadvantages of the geometric deformable models, that is the computational cost, is strongly reduced by the proposed numerical approach which limits the dimensions of the linear systems involved in the solution.

The paper is organized as follows. The non-linear PDE model for tubular structures segmentation is introduced in Section 2, and numerical aspects related to the discretization of the PDE model are discussed in Section 3. The C-segmentation algorithm is discussed in details in Section 4, and the anisotropic variant of the segmentation model is introduced in Section 5. Synthetic as well as real tests are provided in Section 6. Some selected 3D examples are also presented in Section 6 to demonstrate the effectiveness of this technique for automatic segmentation of bloods vessels in volumetric MRA/CTA images. Section 7 contains concluding remarks.

## 2 A Segmentation Model for Tubular Structures

Several recently proposed 3D segmentation methods are based on deformable models, which can naturally capture the physics and geometry of shapes varying in space and time. In this section we formulate the segmentation problem as a special deformation of a 3D manifold driven by the structures we want to recover. Classical segmentation problems show oversmoothed structures and eventually uncomplete boundaries and the surface evolution usually flows over the boundaries of longer and thinner objects when propagating. A common choice to detect structure boundaries and to drive diffusion or segmentation process is the Perona-Malik diffusivity

$$g(s) = 1/(1 + (s/\rho)^2), \tag{1}$$

where $\rho > 0$ is a small positive constant.

For the implicit representation of the segmented surface, we consider a special 3D manifold which is the graph of a trivariate function $\phi$ mapping an open set $\Omega \subset \mathbb{R}^3$ into $\mathbb{R}$. The problem of determining the surface that best fits the object boundary represented in a 3D image $I$, can be posed as a volume minimization problem with objective function

$$V_g := \int_\Omega g(\|\nabla I\|) dV \qquad dV = \sqrt{1 + \|\nabla\phi\|^2} dxdydz, \tag{2}$$

where the metric $g$ is defined by (1) in $\Omega$ and $V_g$ represents the weighted volume of a 3D manifold on $\Omega$.

The volume functional (2) can be minimized and according to the steepest descent, reading $\varepsilon = 1$, we have

$$\frac{\partial\phi}{\partial t} = \sqrt{\varepsilon^2 + \|\nabla\phi\|^2}\nabla. \left( g(\|\nabla I\|) \frac{\nabla\phi}{\sqrt{\varepsilon^2 + \|\nabla\phi\|^2}} \right), \tag{3}$$

or, equivalently, in advection-diffusion form

$$\frac{\partial \phi}{\partial t} = \sqrt{\varepsilon^2 + \|\nabla \phi\|^2} g(\|\nabla I\|) \nabla . \left( \frac{\nabla \phi}{\sqrt{\varepsilon^2 + \|\nabla \phi\|^2}} \right) + \nabla g \cdot \nabla \phi. \tag{4}$$

The PDE model (4), $\varepsilon = 1$, represents the mean curvature motion of the 3D manifold in 4D space with metric $g$. The metric $g$ in (4) is the edge function appropriately chosen so that the object boundaries act as attractors under a particular flow. This term allows us to extract sharp features, such as edges, corners, spikes, and to accelerate the deformation of the initial function. In the evolution of $\phi$ according (4) the 3D manifold assumes constant values for most regions far from the boundaries. The first term in (4) corresponds to a minimal volume regularization weighted by the function $g$, while the second term corresponds to the attraction to the image edges. The advection term in equation (4) introduces a driving force which moves the level surfaces towards the object boundaries.

Equation (3) in case $\varepsilon \in (0, 1]$ is proposed in [2] for dealing with the boundary completion problem. The variability in the parameter $\varepsilon$, $\varepsilon \in (0, 1]$, provides both a regularization effect and a hole filling strategy. The effect of the parameter $\varepsilon$ is to segment boundaries which are eventually uncompleted due to, for example, noise or corruptions in the acquisition phase. However, this does not help in the reconstruction of slightly disconnected tubular structures. The latter problem is solved by the introduction of a suitable diffusion tensor, which is discussed in Section 5.

The starting initial function $\phi_0$ is usually a problem, since it involves user interaction for locating some starting points at one particular recognizable part of the structure to be segmented inside the 3D image. This is overcome by our method which automatically initialize the surface evolution using a suitably designed distance function, as described in Section 4.

We can adapt the PDE model (3) to compute Boolean operations between implicit surfaces $\mathcal{M}_1$ and $\mathcal{M}_2$. This can be carried out quite easily, using the $min$, $max$ tools on the related signed distance functions $dist_1(x)$ and $dist_2(x)$. In fact the union, intersection and differences between two surfaces can be obtained applying the evolving PDE (3) initialized by (9) in Section 4, where $dist(x)$ is defined respectively by

$$\begin{array}{ll} dist(x) = \min\{dist_1(x), dist_2(x)\}, & \textbf{union} \\ dist(x) = \max\{dist_1(x), dist_2(x)\} & \textbf{intersection} \\ dist(x) = \max\{dist_1(x), -dist_2(x)\} & \textbf{difference}(\mathcal{M}_1 - \mathcal{M}_2) \\ dist(x) = \max\{-dist_1(x), dist_2(x)\} & \textbf{difference}(\mathcal{M}_2 - \mathcal{M}_1). \end{array} \tag{5}$$

## 3 Solving the PDE Model

The computational method for solving (3) is based on an efficient semi-implicit co-volume scheme as suggested in [2]. The semi-implicit in time discretization is obtained by treating the nonlinear terms of the equation from the previous

time step while the linear ones are considered at the current time level. Time-discretization of (3) by Euler's method yields the following semi-discrete scheme

*Let $\tau$ be a uniform discrete time step, $\phi_0$ be a given initial function. Then, for every discrete time step $t_n = n\tau$, $n = 1, \ldots N$, we look for a function $\phi^n$, solution of the equation*

$$\frac{1}{\sqrt{\varepsilon^2 + \|\nabla\phi^{n-1}\|^2}} \frac{\phi^n - \phi^{n-1}}{\tau} = \nabla. \left( g^0 \frac{\nabla\phi^n}{\sqrt{\varepsilon^2 + \|\nabla\phi^{n-1}\|^2}} \right), \tag{6}$$

where $g^0 := g(\|\nabla I\|)$.

The computational domain is obtained through $\Omega$-decomposition into cubic cells and the construction of a co-volume mesh using a complementary 3D tetrahedral grid. Following the classical finite volume methodology we integrate (6) over every co-volume $p$, $p = 1, \ldots, M$ and according to the details explained in [2] we get at the time step $n$, a system of linear equations which can be written in matrix-vector form as

$$A\Phi^n = b, \tag{7}$$

where $A \in \mathbb{R}^{M \times M}$ is the coefficient matrix, which is symmetric and diagonally dominant M-matrix, and $\Phi^n = (\phi_1, \ldots, \phi_M)$ is the vector solution. Since the unknown function $\phi(x, t)$ evolves only on nodes sufficiently close to the structure boundary, we speed up the computation by determining the updated values for $\phi(x, t)$ only for the nodes identified by initial function $\phi_0(x) > \eta$, for a given small positive threshold $\eta$.

In case of vessel structures, for example, this means a significant reduction of the computational effort required since the number of nodes representing the vessels is small compared with the dimension of the entire 3D image which contains them. In practice, at each time step, the number of unknowns of the linear system (7) is significatively reduced, and thus both the storage and the computational cost are much lower. Since at each row of $A$ corresponds a node in $\Omega$, if we consider a limited number of nodes $M_1 << M$, we get a linear system with a sparse coefficient matrix of rank $M_1$, which contains $M - M_1$ zero rows and columns. It is easy to verify that if we first apply a suitable permutation of rows and columns of $A$ , and corresponding elements of $b$, we get a linear system with a coefficient matrix $\widetilde{A} \in \mathbb{R}^{M_1 \times M_1}$ with full rank which has the same properties as $A$, that is, it's symmetric and positive definite. In a similar way, the same permutation applied to the components of the right-hand side vector $b$, leads to a vector $\widetilde{b} \in \mathbb{R}^{M_1}$. Therefore, instead of solving the linear system (7) which involves a $M \times M$ coefficient matrix, we can apply the preconditioned conjugate gradient iterative method, using diagonal scaling as preconditioner, for computing the solution $\widetilde{\Phi}$ of the linear system

$$\widetilde{A}\Phi = \widetilde{b}, \tag{8}$$

with a negligible approximation error on the solution.

## 4 The C-Segmentation Algorithm

The C-segmentation procedure consists of two steps: the partitioning phase driven by the Boolean operations to obtain an initial function, and the segmentation phase. The case of segmentation of tubular structures from a single input image is trivially a simplification of the proposed C-segmentation method. In this section, we discuss the implementation of the PDE model (3) for segmentation of multiple 3D images.

Let $\Omega$ be a common support. Each gray-level 3D image $i$ containing tubular structures of interest is thresholded to obtain a rough segmentation estimate which is used to generate an initial distance function. The thresholding process consists of making a binary image $I_i$ from the input $i$ image based on a user threshold. Since the images can be represented by a real-valued function defined on a region $\Omega \subset \mathbb{R}^3$ or by the discretization of such a function, the threshold process let us define in a natural way the sub-domain $\Omega_i \subset \Omega$, $\Omega_i := \{x \in \Omega : I_i(x) = 1\}$. The choice of the threshold value is not an issue due to the fact that in practical cases the structures to be segmented are characterized by a particular intensity value represented by a given gray level. For example, vascular system containing a contrast fluid, can be identified as the brightest formations in the volume. As it will be better illustrated by the examples in Section 6 the 3D mask $I_i$ resulting from the pre-computed binarization, in general, preserves the largest tubular structures while breaks up into small pieces the thinnest ones. These structures will be perfectly recover and reconnected by the surface evolution process.

Each image $i$ has an associated set (region) $\Omega_i$. Depending on the type of the fusion task $\{\Omega_i\}_{i=1,\cdots,S}$, where $S$ is the number of input images, need not be exactly disjoint and/or cover the whole region $\Omega$. The composed signed distance function $dist(x)$ is then obtained by the signed distance functions $dist_i(x), i = 1, .., S$, with respect to $\Omega_i$, following the rules (5).

We define the initial function $\phi_0$ as follows

$$\phi_0(x) = \begin{cases} 1 & \text{if} \quad dist(x) < 0 \\ (1 - \frac{dist(x)}{max\{dist(x)\}}) & \text{else} \end{cases} . \tag{9}$$

The implicit function $\phi_0$ represents the initial surface which continuously evolves, by following equation (3), towards the boundaries of the tubular structures. The evolution is stopped when a change of solution in time (in $L_2$-norm) is less than a prescribed tolerance.

A critical issue is the definition of the composed diffusion function $g(\cdot)$ in (3) when the C-segmentation considers several input images. For example, in case of difference between two images, which are characterized by $g^1$ and $g^2$, the composed diffusion function $g^0$ used in (3) is given by

$$\begin{array}{ll} \text{if} \quad ((g^1 \leq \epsilon)\texttt{and}(g^2 \leq \epsilon) \quad \texttt{or} \quad (g^1 \geq \epsilon)\texttt{and}(g^2 \geq \epsilon)) & g^0 = 1 \\ \text{else} & g^0 = min(g^1, g^2), \end{array} \tag{10}$$

with $\epsilon > 0$, we used $\epsilon = 1 \cdot 10^{-3}$ in the computational examples. We can proceed similarly for other Boolean operations.

Finally, the reconstructed surface is obtained from the implicit surface $\phi$ as the zero level set of the function $\phi(x) - s$, that is the $s$-level set of $\phi$: $\{x \in \Omega : \phi(x) = s\}$, where $s = (max(\Phi) + min(\Phi))/2$. This is motivated by the fact that the flow driven by (3) forms a sharp step in the proximity of the object boundaries, while it approaches at constant values inside/outside the object.

## 5 An Anisotropic Variant of the Segmentation Algorithm

In this section we provide a variant of the isotropic model (3) designed to improve significantly the connectivity of the coherent structures in the segmentation. The idea is to incorporate local orientation of the tubular structures into the dynamic segmentation process in such a way that at each time step the surface evolves by isotropic mean curvature motion in homogeneous regions, while it is driven by the directional field representing the orientation of the tube in presence of tubular structures. We aim to capture the vessel's structure and the vessels directions locally by a local spatial coherence descriptor. Coherence enhancing image smoothing has been introduced by [3] and successfully applied in image filtering by anisotropic diffusion. This type of nonlinear diffusion includes the construction of a diffusion tensor which is built as follows. Given an image $I$, and its Gaussian-smoothed version $\nabla I_\sigma$, a regularized shape descriptor is provided by

$$J_\delta(\nabla I_\sigma) := (K_\delta * (\nabla I_\sigma \otimes \nabla I_\sigma)) \tag{11}$$

where $K_\delta$ is a Gaussian kernel with $\delta \geq 0$. The matrix $J_\delta$ is symmetric positive semi-definite and its eigenvalues $\mu_1 \geq \mu_2$ integrate the variation of the gray values within a neighborhood of size $O(\delta)$. They describe the average contrast in the corresponding eigendirections $\mathbf{v}_1$ and $\mathbf{v}_2$. The orientation of the eigenvector $\mathbf{v}_2$, corresponding to the smaller eigenvalue, represents the direction of lowest fluctuations, the so-called coherence orientation. In this way, constant areas are characterized by $\mu_1 = \mu_2 = 0$, while straight edges give $\mu_1 \gg \mu_2 = 0$.

The normalized coherence value which measures the anisotropic structures within a window of scale $\delta$ is thus defined as

$$c = \frac{(\mu_1 - \mu_2)^2}{\max\{(\mu_1 - \mu_2)^2\}}, \quad c \in [0, 1]. \tag{12}$$

Thus $c$ approaches to 1, for anisotropic structures and tends to zero for isotropic structures.

The diffusion tensor $D$ is a matrix with the same eigenvectors as the (regularized) structure tensor $J_\delta$ and its eigenvalues are given by

$$\begin{aligned} \lambda_1 &= g(\|\nabla I\|) \\ \lambda_2 &= \begin{cases} g(\|\nabla I\|) & \text{if} \quad \mu_1 = \mu_2 \\ g(\|\nabla I\|) + (1 - g(\|\nabla I\|))e^{-\kappa/c} & \kappa > 0, \text{ else} \end{cases} \end{aligned} \tag{13}$$

where $g(\cdot)$ is the composed diffusion function, defined for example, by (10) which suitably adapts its values to the anisotropy. The parameter $\kappa$ has the role of a

threshold, and $c$ is the coherence defined in (12). Therefore, the matrix $D$ has the following form

$$D = [\,\mathbf{v}_1\ \mathbf{v}_2\,] \begin{bmatrix} \lambda_1 & 0 \\ 0 & \lambda_2 \end{bmatrix} \begin{bmatrix} \mathbf{v}_1^T \\ \mathbf{v}_2^T \end{bmatrix}. \tag{14}$$

In local homogeneous areas of an image the diffusion is reduced to be the isotropic mean curvature motion driven by (3), in fact we have $D = g(\|\nabla I\|)$. Areas nearby elongated structures are characterized by values of $g(\cdot)$ approaching to zero, which gives $\lambda_2 >> \lambda_1$. The effect on the diffusion of the segmentation function is thus stronger along the coherence directions. In all the experiments reported in Section 6 we set $\kappa = 1 \cdot 10^{-5}$. Since if $c >> \kappa$ then $\lambda_2 \approx 1$, while if $c << \kappa$ then $\lambda_2 \approx g(\|\nabla I\|)$, the segmentation function flows along the coherence direction when it approaches to the edges and stops when the object boundary is reached. The incorporation of the diffusion tensor $D$ defined by (14) in the segmentation model (3) leads to the following nonlinear anisotropic segmentation

$$\frac{\partial \phi}{\partial t} = \sqrt{\varepsilon^2 + \|\nabla \phi\|^2}\nabla . \left( D \frac{\nabla \phi}{\sqrt{\varepsilon^2 + \|\nabla \phi\|^2}} \right), \quad \phi(x,0) = \phi_0(x) \quad x \in \Omega. \tag{15}$$

We will refer to the models (3) and (15) by isotropic and anisotropic segmentation models, respectively. The PDE model (15) can be easily extended to 3D or 4D segmentation problems; we refer the reader to [1] for the numerical aspects involved in the discretization of the diffusion tensor.

## 6 Results and Experiments

We tested the performance of the proposed C-segmentation method on 2D/3D synthetic and real examples. Example 1 and 2 demonstrate the performance of the anisotropic C-segmentation model compared with the isotropic one to verify the important role of the diffusion tensor in the segmentation of tubular structures. Examples 3, 4 and 5 illustrate results from the application of composed segmentation of 2D/3D images. For all the experiments, we apply C-segmentation algorithm as illustrated in Section 4, with or without diffusion tensor, and we set the time step parameters involved to $\tau = 1 \cdot 10^{-3}$, for 3D images and $\tau = 1 \cdot 10^{-2}$ for the 2D images, and $\varepsilon = 1 \cdot 10^{-3}$ in (3). We stop the iterations when the change of solution in time is less than $1 \cdot 10^{-4}$. In our experiments, the segmentation of images with high contrast (see Examples 2 and 3) provides good results when an automatic choice for parameter $s$ is chosen such as $s = (max(\Phi) + min(\Phi))/2$, while in case of images like in Examples 1, 4 and 5, the results are more sensitive to the choice of $s$, and visual inspection could be required to tune the automatic choice of $s$.

*Example 1.* In the first 2D example we consider the segmentation of a carotid vascular system represented in a Magnetic Resonance Angiography (MRA) image of $182 \times 182$ pixels shown in Fig. 1 (left). MRA is based on detection of signals from flowing blood and suppression of signals from other, static, tissues.

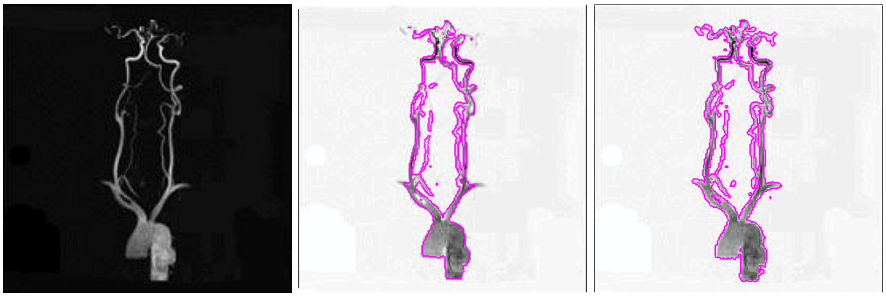

**Fig. 1.** Carotid vascular system segmentation; the original image (left); results of the isotropic model (center), and anisotropic model (right)

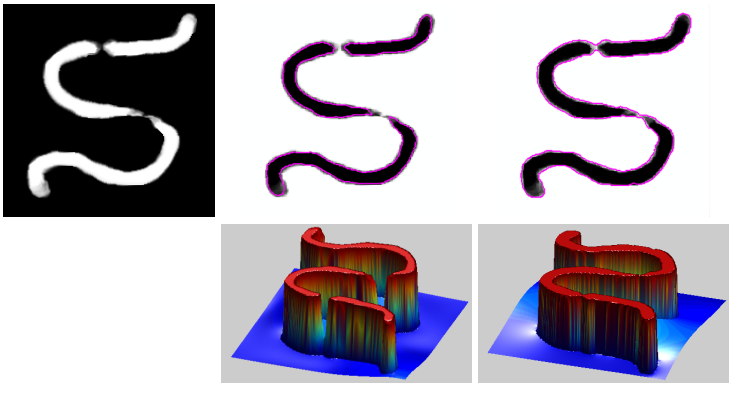

**Fig. 2.** First row: original synthetic image (left); results obtained by the isotropic (left) and anisotropic segmentation model (right). Second row: associated segmentation function $\phi$ is shown at the final time step of isotropic (left) and anisotropic segmentation (right).

The blood vessels appear as high intensity regions in the image. The structures to be segmented represent several vessels of variable diameters which are close to each other, partial occlusions and intersections make the segmentation very challenging. In Fig.1 the segmented structures obtained by 10 iterations of the isotropic (center) and anisotropic (right) segmentation models are displayed. The boundary curves in pink color are extracted using contour values $s = 0.90$ and $s = 0.98$, respectively. Visual comparison shows the anisotropic segmentation method to give the most accurate restoration.

*Example 2.* The second example illustrates the ability to reconstruct structures which present small occlusions along the coherence direction. The synthetic image to be segmented of dimension $200 \times 200$ pixels is shown in Fig. 2 (first row, left). Applying 10 time steps of the anisotropic segmentation model, the structure is well reconstructed while maintaining the narrowing, as shown in Fig.2

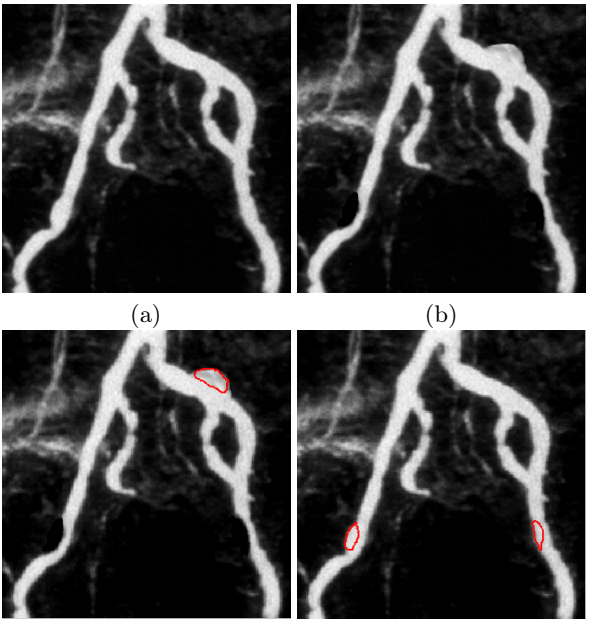


**Fig. 3.** C-segmentation of images (a) and (b). Result in (c) of $(b)\backslash(a)$ and in (d) of $(a)\backslash(b)$.

(first row, right). The propagation driven by the isotropic segmentation model leads to enhance the disconnections, as shown in Fig.2 (first row, center). The boundary curves determined as iso-contours of the segmentation functions shown in Fig.2 (second row), using $s = 0.95$ are over-imposed on the original image and shown in Fig.2 (first row).

*Example 3.* Verification of the proposed C-segmentation method is carried out on a real echo image show in Fig.3 (a) where we generated one synthetic bump and two synthetic holes, simulating aneurysm and stenosis effects, as illustrated in Fig.3 (b). Applying C-segmentation to the Boolean difference $(b) \setminus (a)$ we are able to enhance the aneurysm as shown in Fig.3 (c), while to detect the stenosis effects we apply C-segmentation to the Boolean difference $(a) \setminus (b)$, obtaining the results illustrated in Fig.3 (d).

*Example 4.* Volumetric segmentation is applied to a Computed Tomographic Angiography (CTA) data set shown in Fig.4(left). The volumetric data set `kidney` of dimension $201 \times 201 \times 201$ has been extracted from a $436 \times 436 \times 540$ CTA image of the kidney vasculature system and present vessel patterns with different curvatures, diameters and bifurcations. The final segmentation obtained after 10 time steps of the segmentation algorithm is shown in Fig.4(right).

*Example 5.* The last experiment demonstrates the performance of the proposed technique to segment a complex structure extracted from two overlapping 3D

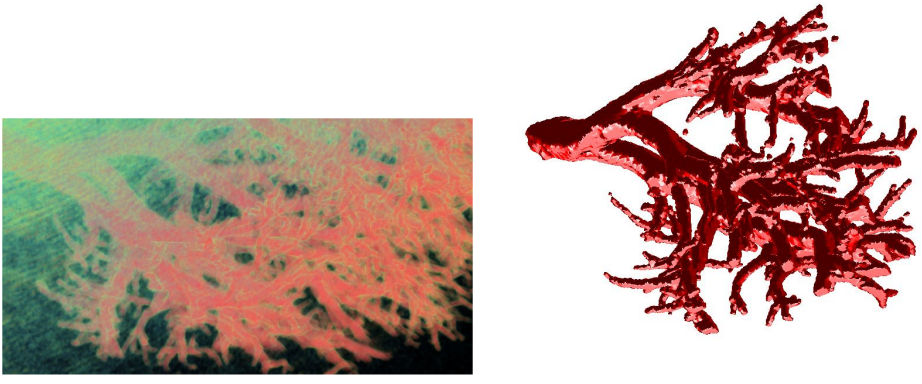

**Fig. 4.** Segmentation of the `kidney` volume data set: (left) original CTA image (right) segmentation result

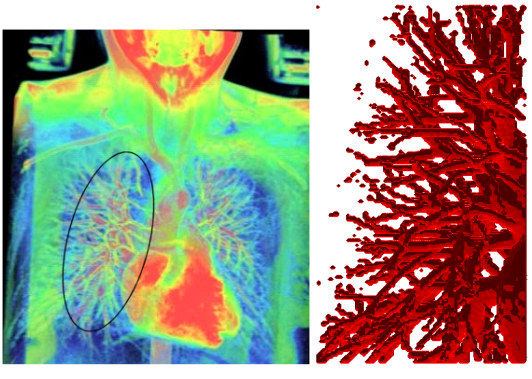

**Fig. 5.** Segmentation of the `lung` volume data set: (left) original MRA image, (right) C-segmentation result

MRA images representing the airway tree of a human lung. The original MRA image is illustrated in Fig.5(left) using volume rendering. In particular the ellipsoidal area outlined in the image includes the region of interest for segmentation inside the `lung` image. The data set `lung` is DICOM format and sample images available on the web site (`http://www.osirix-viewer.com/Downloads.html`). We simulated the acquisition of two partially overlapping 3D MRA images covering the area of interest consisting of $156 \times 156 \times 156$ voxels each, and we applied the C-segmentation algorithm using union Boolean composition. Fig.5(right) shows the obtained single one segmentation of the human airway tree, where several branching generations were detected.

These preliminary results demonstrate the applicability of the developed method for the C-segmentation of quite different and topological complex tubular structures.

## 7 Conclusions

In this paper we introduced the C-segmentation method based on the distance function which is successfully applied to 2D/3D images containing tubular structures. The algorithm is automatic, accurate and fast. The latter is due to a speed up strategy in the iterative method for linear systems. The algorithm is provided with a diffusion tensor to move the evolving surface toward elongated tubular structures, connecting gaps in the underlying raw data, while keeping the structures distinguished along the coherence direction. This model defines a general segmentation framework which combines object information from different images into any logical combination, rather than following the difficult a posteriori process to compose segmentation results obtained separately.

## Acknowledgments

This work has been supported by PRIN-MIUR-Cofin 2006, project and by University of Bologna "Funds for selected research topics".

## References

1. Drblikova, O., Mikula, K.: Semi-implicit Diamond-cell Finite volume Scheme for 3D Nonlinear Tensor Diffusion in Coherence Enhancing Image Filtering. In: Eymard, R., Herard, J.M. (eds.) Finite Volumes for Complex Applications V: Problems and Perspectives, ISTE and WILEY, London, pp. 343–350 (2008)
2. Corsaro, S., Mikula, K., Sarti, A., Sgallari, F.: Semi-implicit covolume method in 3D image segmentation. SIAM J. Sci. Comput. 28(6), 2248–2265 (2006)
3. Weickert, J., Scharr, H.: A scheme for coherence enhancing diffusion filtering with optimized rotation invariance. Journal of Visual Communication and Image Representation 13(1/2), 103–118 (2002)
4. Kirbas, C., Quek, F.: A review of vessel extraction techniques and algorithms. ACM Computing Surveys 36(2), 81–121 (2004)
5. Hassan, H., Farag, A.A.: Cerebrovascular segmentation for MRA data using levels set. International Congress Series, vol. 1256, pp. 246–252 (2003)
6. Scherl, H., et al.: Semi automatic level set segmentation and stenosis quatification of internal carotid artery in 3D CTA data sets. Medical Image Analysis 11, 21–34 (2007)
7. Cohen, L.D., Deschamps, T.: Segmentation of 3D tubular objects with adaptive front propagation and minimal tree extraction for 3D medical imaging. Computer Methods in Biomechanics and Biomedical Engineering 10(4), 289–305 (2007)
8. Gooya, A., Liao, H., et al.: A variational method for geometric regularization of vascular segmentation in medical images. IEEE Transaction on image processing 17, 1295–1312 (2008)
9. Sandberg, B., Chan, T.F.: A logic framework for active contours on multi-channel images. J. Vis. Commun. Image R. 16, 333–358 (2005)
10. Westin, C.-F., Lorigo, L.M., Faugeras, O.D., Grimson, W.E.L., Dawson, S., Norbash, A., Kikinis, R.: Segmentation by Adaptive Geodesic Active Contours. In: Delp, S.L., DiGoia, A.M., Jaramaz, B. (eds.) MICCAI 2000. LNCS, vol. 1935, pp. 266–275. Springer, Heidelberg (2000)